Effects of aluminum content on thermoelectric performance of Al$_x$CoCrFeNi high-entropy alloys

Md Abdullah Al Hasan [a], Jiaqi Wang [a], Seungha Shin [a,*], Dustin A. Gilbert [b,c], Peter K. Liaw [b], Nan Tang [b], W.L. Namila C. Liyanage [c], Louis Santodonato [b,d], Lisa DeBeer-Schmitt [d], Nicholas P. Butch [e,f]

[a] Department of Mechanical, Aerospace, and Biomedical Engineering, The University of Tennessee, Knoxville, TN, USA
[b] Department of Materials Science and Engineering, The University of Tennessee, Knoxville, TN, USA
[c] Department of Physics and Astronomy, The University of Tennessee, Knoxville, TN, USA
[d] Neutron Scattering Division, Oak Ridge National Laboratory, Oak Ridge, TN 37831, USA
[e] National Institute of Standards and Technology Center for Neutron Research, Gaithersburg, MD 20878, USA
[f] University of Maryland, College Park, College Park, MD 20742, USA

ARTICLE INFO

ABSTRACT

Introducing a non-regular distribution in the mass and bonding by including distinctly different elements can reduce the phonon transport even within structurally well-ordered materials. These distributions are a quality of all high-entropy alloys (HEAs), however the inclusion of aluminum in Al$_x$CoCrFeNi is particularly impactful due to the large mismatch in atomic mass with other components. The resultant low phonon conductivity is a requirement for high thermoelectric performance, motivating the investigation of the effects of Al content on phonon transport as well as other thermoelectric properties. This work examines the phonon and electron transport and thermoelectric conversion properties with various Al contents ($0 \leq x_{Al} \leq 2$) in this Cantor alloy using first-principles calculations, molecular dynamics, and semi-classical Boltzmann transport theory. The calculated phonon density of states and thermoelectric properties present reasonable agreements with experiments, including neutron scattering. A large reduction of phonon conductivity (k_L) is observed even with low x_{Al}s, which we attribute to effective phonon scatterings by the large mass mismatch. However, its temperature dependence is not significant, demonstrating a minor contribution of interphonon scattering. In contrast, electrical conductivity (σ) and Seebeck coefficient (S) increase with temperature at higher x_{Al}s with body-centered cubic structures. Therefore, the thermoelectric figure of merit (ZT) of Al$_x$CoCrFeNi HEAs is enhanced by increasing the Al content mainly due to the increase of the thermoelectric power factor (σS^2) at high temperatures, while at low temperatures the phonon-scattering enhancement by mass mismatch is also important.

© 2021 Elsevier B.V. All rights reserved.

1. Introduction

Thermoelectric materials have attracted enormous attention over the past decades due to their potential applications in the recovery of waste heat, providing cleaner energy and reducing greenhouse gas emissions [1–5]. Generally, the energy conversion efficiency in thermoelectric materials is determined by the figure of merit [6], $ZT = S^2\sigma T/(k_e + k_L)$, where S is the Seebeck coefficient, σ the electrical conductivity, k_e the electronic thermal conductivity, k_L the lattice thermal conductivity, and T the temperature; the higher ZT, the more efficient thermoelectric energy conversion [6,7]. Therefore, suppressing thermal conductivity, while maximizing Seebeck coefficient and electrical conductivity, leads to a high figure of merit (ZT). However, the interdependence of these properties imposes a challenge on identifying efficient thermoelectric materials. Specifically, as the electron contribution to thermal transport dominates over phonon or atomic vibration in metallic materials, higher σ causes higher k. Semi-metals and semi-conductors have been broadly demonstrated as thermoelectrics, and high ZT values of Bi$_2$Te$_3$, PbTe, and (Bi$_{1-x}$Sb$_x$)$_2$(Se$_{1-y}$Te$_y$)$_3$ (based on p-block elements) have been reported [8]. However, these materials contain toxic or scarce elements, which are not suitable for scalable production, and quickly degrade at high temperatures ($T > 800\ °C$) [7–9]. Although half-Heusler type materials show high enough ZT (≈ 1) values at high

temperatures that can compete with the state-of-the-art *n*-type SiGe compounds, they include expensive metals, such as Hf or Pd (i.e., corresponds to 90% of the total material cost), which hampers their commercial use [8,10,11]. Furthermore, some half-Heusler compounds are effective only at low *T*s (< 650 K) [12].

High-entropy alloys (HEAs) have been regarded as novel types of alloys because of their unique microstructures and adjustable properties [13–16]. In HEAs, five or more elements are mixed with equimolar or near-equimolar atomic fractions, each ranging from 5 to 35 at. percent (at%) [17]. Thus, the high configurational entropy of mixing, especially at elevated temperatures, can thermodynamically stabilize solid solution alloys, and their complex phase space enables exceptional properties, including mechanical properties [13,15,18]. A recent study on HEAs reveals their promising features for high-*T* thermoelectric applications [8]. In HEAs, complexity through severe lattice distortions, point defects, and the precipitation of secondary phases enhance the phonon scattering, reducing lattice thermal conductivity, while maintaining a high mobility of the conduction electrons [8]. Furthermore, the high symmetry of crystal structures, such as body-centered-cubic (BCC) and face-centered-cubic (FCC) phases, in HEAs allows for a high convergence of the bands that are close to the Fermi level to obtain a high Seebeck coefficient [19]. However, due to the involvement of many complexities (i.e., disorder, high compositional entropy, mass and interaction mismatches) in HEAs, tuning of the thermoelectric properties remains a great challenge [8]. Therefore, a comprehensive study is required for the reduction of thermal conductivity and enhancement of desirable properties, i.e., Seebeck coefficient and electrical conductivity.

Different from other HEAs composed of elements with similar atomic mass, the Al in $Al_x CoCrFeNi$ has an atomic mass (m_{Al} = 26.98 g/mole) which is 52% smaller than the average mass of other elements ($m_{avg,others}$ = 56.37 g/mole) while the other elements have atomic masses within 8% of this average. This large distribution of atomic mass causes a significant increase of phonon scattering, reducing the lattice thermal conductivity. Thus, we can expect that more enhanced thermoelectric performance (or higher *ZT*) can be achieved via effective thermal transport control by the Al content (x_{Al}) in $Al_x CoCrFeNi$ HEAs. However, the Al content also influences other properties of $Al_x CoCrFeNi$, including the crystal structure, mechanical, electrical, magnetic, anticorrosive, and thermodynamic properties [20–24]. Therefore, the study of $Al_x CoCrFeNi$ for thermoelectric performance requires comprehensive understanding of the Al content effects on various properties that contribute to the thermoelectric efficiency. Only a few experimental studies have been performed on the thermoelectric properties of $Al_x CoCrFeNi$; for example, Shafeie et al. [8] reported electrical conductivity (σ), Seebeck coefficient (S), thermal conductivity (k), power factor (σS^2), and figure of merit (ZT) for $0 \leq x_{Al} \leq 3$ in the temperature range of 100–900 °C. However, to our best knowledge, comprehensive computational study has not been found yet.

Through effective parametric control, computational approaches can facilitate the identification of effects of a specific control parameter on material properties. For multi-component alloy systems, several computational studies have been successfully performed to investigate the effects of element concentration. For example, first-principles calculations have been employed to study the effect of Mn and Al contents on the elastic properties, structural stability, and magnetic properties of FeCoNi-based alloys [25], BCC $Al_x Hf_{1-x}NbTa$-TiZr [26], and $Al_x CrMnFeCoNi$ HEAs [27]. This research aims to identify the effects of Al content on thermoelectric performance of $Al_x CoCreFeNi$ HEAs ($0 \leq x_{Al} \leq 2$), the lattice thermal conductivity (k_L), electronic transport (σ and k_e), thermoelectric conversion coefficient (S), etc. over a wide temperature range (300–1200 K) using molecular dynamics (MD), density functional theory (DFT),

and the Boltzmann transport theory. Simulation results are compared with the experimentally measured phonon density of states.

2. Methodology

The atomic structures of the examined $Al_x CoCrFeNi$ HEAs present stable crystalline orders over the temperature range of 300–1200 K. Previous experimental works have shown that the stable phase of the HEAs changes from FCC to BCC structures as the Al content (x_{Al}) increases [20,24,28]. In the current research, the crystalline structure and the lattice constant were determined by a minimum energy calculation in MD and DFT. In these models, the initial structures were created via random and uniform distribution of the constituent elements (Al, Co, Cr, Fe, and Ni) in the simulation space according to the corresponding Al concentration of each HEA, as shown in Fig. 1a [29]. Nine Al concentrations were modeled, which result in the atomic number ratio Al:Co:Cr:Fe:Ni of x_{Al}:1:1:1:1, where x_{Al} = 0, 0.3, 0.5, 0.75, 0.875, 1, 1.25, 1.5, and 2.

Among the properties for thermoelectric performance, the phonon contribution to thermal transport in $Al_x CoCrFeNi$ was investigated, using classical MD simulations. A phonon spectrum (density of states, D_p) was also calculated to validate the MD simulations by comparing with experimental values and to understand the change in phonon transport. In the classical MD simulations, the interactions in the Al-Cr-Co-Fe-Ni elements were calculated employing the embedded atom model (EAM) potential [30,31]. The EAM potentials have been widely employed to simulate various metallic processes in atomic scale and found successful in capturing many-body effects of metallic bonding [30–33]. Newton's equations of motion were integrated using the Verlet algorithm [34] with a time-step of 0.5 fs. Modeling was repeated with at-least five different initial structures for each Al concentration to verify the lattice-constant and crystal-order determinations. To examine the mass-mismatch effect on the phonon properties (i.e., the phonon density of state and lattice thermal conductivity) of the HEAs, a second series of simulations were performed, which assigned the mass of Al to match the average of the other elements, 56.367 g/mole. An energy minimization using the conjugate gradient (CG) algorithm [35] with a force and energy precision of 1.0×10^{-10} eV/Å was applied to the initial structures. Comparing the respective energy values of FCC and BCC cases, the crystal order of the lower energy value was determined for each Al concentration.

Phonon density of states (D_p) is calculated using the Fourier transform of the velocity autocorrelation function from the MD simulations [36]. The velocity data for the D_p calculations were obtained from simulations with $10 \times 10 \times 10$ supercells of an FCC or BCC lattice containing 4000 or 2000 of randomly distributed Al, Co, Cu, Fe, and Ni atoms. A canonical ensemble (*NVT*; constant number of atoms, volume, and temperature) with Nosé thermostats was employed, and the last 50 ps of simulation data were used for the velocity autocorrelation.

To validate the calculated D_p from MD, we also measured D_p via neutron scattering experiments. Polycrystalline ingots of the proposed HEA compositions were prepared by arc melting and subsequent annealing as described previously [23], and a 1 cm diameter × 1 cm tall cylinder was cut from the ingot. The D_p of the prepared sample was measured on the Disc-Chopper Spectrometer (DCS) at the National Institute for Standards and Technology. Measurements were performed by heating the sample to 500 K in vacuum then illuminating it with 2.5 Å wavelength neutrons; using a time-of-flight scheme the change in the kinetic energy of the neutron after scattering is determined. Since the samples are polycrystalline, the diffraction pattern from the scattering appears as a ring, which is integrated to resolve scattering intensity versus
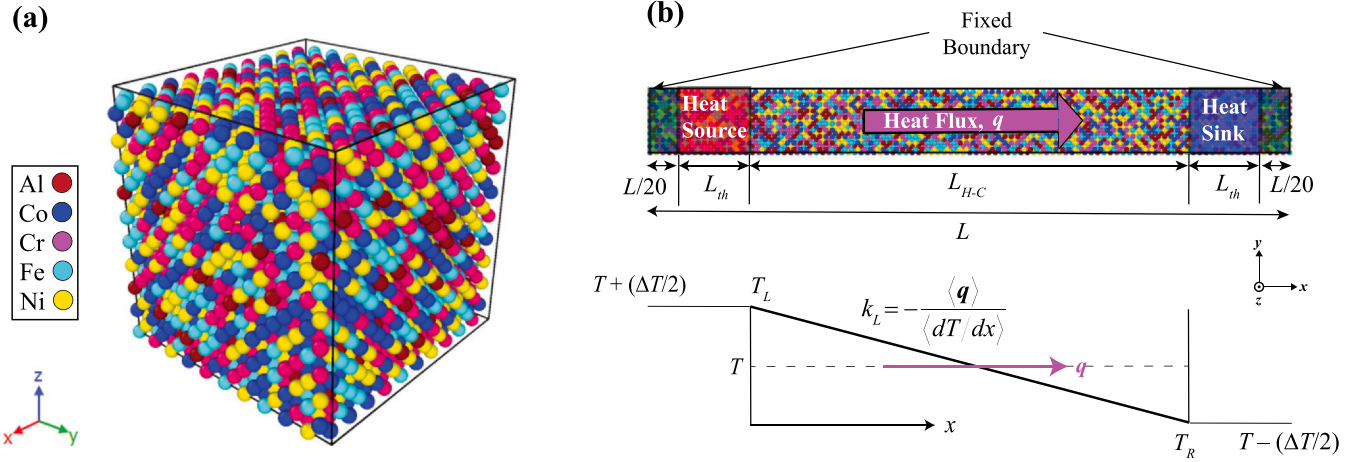
(a)

(b)

Fig. 1. (a) 10 × 10 × 10 supercell for energy and phonon spectrum analysis via classical MD simulations, and (b) non-equilibrium MD simulation setup for the lattice thermal conductivity calculation with a 100 × 10 × 10 supercell. (For interpretation of the references to color in this figure legend, the reader is referred to the web version of this article.)

momentum transfer vector (q) and the change in the neutron energy. The one-dimensional generalized density of states is generated by integrating the scattering intensity across all q; the scattering intensity is corrected for the Fresnel decay and a Boltzmann factor representing an activation probability. Results were analyzed using the DAVE software package [37].

The lattice thermal conductivity of $Al_xCoCrFeNi$ HEAs (k_L) is examined by analyzing the heat flow and temperature distributions generated by a non-equilibrium temperature setup in MD. 100 × 10 × 10 supercells (40,000 atoms for FCC and 20,000 atoms for BCC structures) are created for the nonequilibrium MD simulations. A non-periodic and fixed boundary condition is applied to the x direction, while periodic boundary conditions are to the y and z directions. To achieve fixed boundary conditions in the transport direction (x-direction), we fixed a few layers of atoms at the both ends of the HEA length ([0, $L/20$]gt and [19$L/20$, L], where total length, L = 100a, and a is the lattice constant), as shown in Fig. 1b. Then, next to the both fixed layers, hot (heat source, T_L) and cold (heat sink, T_R) thermostats are applied within a length of L_{th} = $L/10$ (red and blue shades in Fig. 1b, respectively). The system length (L_{H-C}) is defined by the distance between two thermostats. To calculate thermal conductivity at T, ($T + \Delta T/2$) and ($T - \Delta T/2$) are prescribed to the hot and cold thermostat regions, and ΔT = 100 K was employed over the examined temperature range to observe a clear temperature gradient. For the calculation of a heat flux (q, W/m²) and temperature gradient (∇T, K/m), we employed 5 ns of simulation data, which ensure small enough fluctuations in the calculation. Then, the lattice thermal conductivity is calculated, using Fourier's law (k_L = -q/ ∇T) [38].

The electronic-band structures of $Al_xCoCrFeNi$ for thermoelectric properties involving electrons (e.g., k_e, σ_e, and S) are obtained from first-principles calculations, employing DFT. All the DFT simulations in the current research were performed, using the Vienna ab simulation package (VASP) [39] with the projector augmented wave (PAW) potentials [40]. The electronic exchange-correlation interaction was treated by the Perdew-Burke-Ernzerhof (PBE) functional with the generalized gradient approximation (GGA) [41]. The Methfessel-Paxton technique [42] was adopted with a smearing parameter of 0.2 eV. The plane-wave energy cutoff was set to 400 eV, and the electronic-energy convergence criterion to 10^{-4} eV. A 2 × 2 × 2 Γ-centered k-point mesh, which leads to 8 κ-points, was used to conduct the integration over the Brillouin zone. For a wide temperature range of 300–1200 K, we employed molecular dynamics, using the force field from DFT calculations, i.e., ab initio MD (AIMD). 3 × 3 × 3 FCC (108 atoms) and 4 × 4 × 4 BCC (128 atoms)

supercells were created for AIMD. Using a canonical ensemble, *NVT* (i.e., constant number of atoms, volume, and temperature) with temperature control by the Nosé thermostats [43], the atomic position and velocity data were updated with a single time step of 0.5 fs, and 4000 time step data were used for the analysis.

The AIMD results were then processed to evaluate the thermoelectric properties for $Al_xCoCrFeNi$ ($0 \le x_{Al} \le 2$), using the Boltzmann transport theory. The transport coefficients, i.e., electrical conductivity (σ), Seebeck coefficient (S), and electronic thermal conductivity (k_e) tensors, can be calculated as a function of the temperature (T) and chemical potential (μ) by integrating the transport distribution function ($\bar{\sigma}_{\alpha\beta}$) [1,44,45]:

$$\sigma_{\alpha\beta}(T, \mu) = \frac{1}{\Omega} \int \bar{\sigma}_{\alpha\beta}(E) \left[-\frac{\partial f_{FD}(T, E, \mu)}{\partial E} \right] dE, \tag{1}$$

$$S_{\alpha\beta}(T, \mu) = \frac{1}{e_c T \Omega \sigma_{\alpha\beta}(T, \mu)} \int (E - \mu) \bar{\sigma}_{\alpha\beta}(E) \left[-\frac{\partial f_0(T, E, \mu)}{\partial E} \right] dE, \tag{2}$$

and

$$k_{e,\alpha\beta}(T, \mu) = \frac{1}{e_c^2 T} \int (E - \mu)^2 \bar{\sigma}_{\alpha\beta}(E) \left[-\frac{\partial f_0(T, E, \mu)}{\partial E} \right] dE, \tag{3}$$

where Ω, f_{FD}, and e_c are the unit cell volume, the carrier Fermi-Dirac distribution function, and the electron charge, respectively. α and β are tensor indices, and the transport distribution function is defined as

$$\bar{\sigma}_{\alpha\beta}(E) = \frac{e_c^2}{N} \sum_{i,\kappa} \tau u_\alpha(i, \kappa) u_\beta(i, \kappa) \frac{\delta(E - E_{i,k})}{\delta(E)}, \tag{4}$$

where $u_\alpha(i, \kappa)$ is the α-th component of the group velocity, $u(i, \kappa)$, of carriers, N is the number of sampled κ points, i is the band index, and κ is the wave vector. The group velocity can be derived from the band structure by:

$$u(i, \kappa) = \frac{1}{\hbar} \nabla_\kappa E_{i,\kappa}, \tag{5}$$

where $\hbar$ is the reduced Planck constant.

Here, we fit the band structure data into the semi-classical Boltzmann transport theory, which is carried out via the BoltzTraP package [44]. Then, the thermoelectric properties of the HEAs are calculated, using Eqs. (1)–(5), based on their band structures. In the calculations of transport, the distribution function, the carrier relaxation time, τ, is a required input. For simplicity, we approximated its value to a constant (single relaxation time approximation or

SRTA), using the experimental data for these HEAs that are available in the literature [8,22]. Then, the transport properties (i.e., electrical conductivity, electronic thermal conductivity, etc.) are calculated with respect to the relaxation time. On the other hand, the Seebeck coefficient is independent of τ, assuming isotropic relaxation [44] and can be directly obtained using only the band-structure information. This approach has been adopted by several researchers previously and successfully employed to evaluate electrical transport properties of thermoelectric compounds [46,47].

3. Results and discussion

Prior to classical MD simulations for the phonon transport analysis, the crystal structure and lattice parameter for each HEA were evaluated by finding a minimum-energy atomic structure. In Al$_x$CoCrFeNi HEAs, due to the smaller atomic mass and larger size, compared to other constituents, the Al content plays an important role in the structural configuration [24,48–51]. Our simulations confirm the dependence of Al content on the HEA structure, and single FCC and BCC phases are observed for $0 \leq x_{Al} \leq 0.75$ and $0.875 \leq x_{Al} \leq 2$, respectively.

The lattice constants corresponding to the minimum energy states after relaxation are used to create the initial atomic structures for further simulations. The lattice constants and phases from the simulations agree well with the experimental values [20,24] as shown in Fig. 2a, validating the use of classical MD modeling in this work, including the interatomic potential. In general, increasing x_{Al} results in a larger lattice constant, increasing the average atomic volume (or reducing the atomic density), and especially, a large volume expansion is observed in the FCC-BCC transition as exhibited in Fig. 2b. Additionally, the addition of Al atoms reduces the average atomic mass (m_{avg}), while increasing the standard deviation (m_{std}) of the atomic-mass distribution.

The simulated and experimentally measured phonon density of states (D_p) for AlCoCrFeNi are shown in Fig. 3a and demonstrate good agreement in their major peaks and overall shape. This agreement demonstrates that our simulation model accurately describes the phonon behavior, which also supports the calculation accuracy of the lattice thermal conductivity. We also calculated the element-specific contributions to D_p ($D_{p,i}$, where i = Al, Co, Cr, Fe, and Ni), as shown in Fig. 3b. These plots show that $D_{p,Al}$ tends to peak at a much higher energy, ≈ 45 meV, compared to its heavier counterparts (Co, Cr, Fe, and Ni), which share similar peak positions at ≈ 20 meV. The higher-energy peak in Al can be attributed to the light mass of

the Al atoms. The reduced overlap between $D_{p,Al}$ and the other $D_{p,i}$ tends to cause scattering of the phonons, rather than long-range coherent transport; suppression of coherent phonon transport directly corresponds to poor lattice thermal conductivity. A larger x_{Al} shifts of D_p to higher phonon energy (Fig. 3c). However, as Fig. 3d shows, no shift is observed when the mass mismatch of Al is excluded, that is, setting the mass of Al to match the average mass of the other elements (56.367 g/mole). In addition, the transition to a BCC phase at larger x_{Al} causes lower D_p at low energy, which can reduce heat capacity and possibly contribute to further reduction of the lattice thermal conductivity.

The lattice thermal conductivities (k_L) of Al$_x$CoCrFeNi from NEMD simulations at 300 K appear in the range of 2.88–7.43 W/m-K at different Al contents ($0 \leq x_{Al} \leq 2$), as shown in Fig. 4a. This range is in good agreement with the experimental values of k_L for Al$_x$CoCrFeNi [24]. Unlike other metallic materials, the phonon contribution to the thermal conductivity is comparable to the electronic contribution in the HEAs [22,24,52]. Therefore, the k_L control is important for the thermoelectric performance, especially at low temperatures. These calculated results in Fig. 4a present that small inclusions of Al initially cause a large reduction in k_L, however, with further inclusion the reduction is much less; a dramatic drop in k_L occurs at the FCC to BCC structural phase transition ($x_{Al} \sim 0.8$). Removing the mass effect, by setting the mass of the Al to 56.367 g/mole, we observe larger k_L values at all nonzero Al contents (x_{Al}), compared to the simulations employing actual Al mass ($m_{Al} = 26.982$ g/mole), and this difference is more significant at lower x_{Al}s. These results show the critical impact of the mass mismatch, but also implicate the role of scattering from another mechanism – lattice mismatch and a distribution in bonding strength [53].

According to the kinetic theory [54], k_L is inversely proportional to the total phonon scattering rate, which includes the scattering by Al and other scattering mechanisms (e.g., scattering by other phonons, boundaries, electrons, etc.) represented by $\dot{\gamma}_{Al}$ and γ_{others}, respectively,

$$k_L \propto \frac{1}{\dot{\gamma}_{Al} + \gamma_{others}} \qquad (6)$$

Higher x_{Al} leads to more phonon scattering, i.e., larger $\dot{\gamma}_{Al}$, by mass and lattice mismatch, thus reducing k_L. The considerable k_L reduction observed in our simulations confirms Al is an effective phonon scatterer. The modeling shows the critical impact of mass
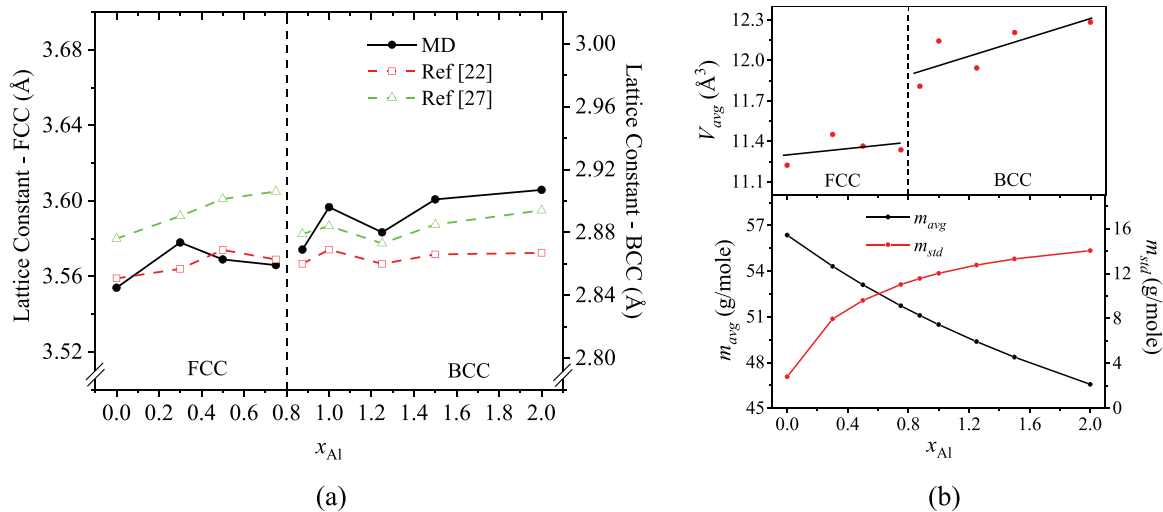

Fig. 2. (a) Lattice constants of Al$_x$CoCrFeNi ($0 \leq x_{Al} \leq 2$) from classical MD and experiments at room temperature (300 K) [20,24] and (b) average atomic volume (V_{avg}), mass (m_{avg}), and standard deviation (m_{std}) of atomic mass with respect to x_{Al}.
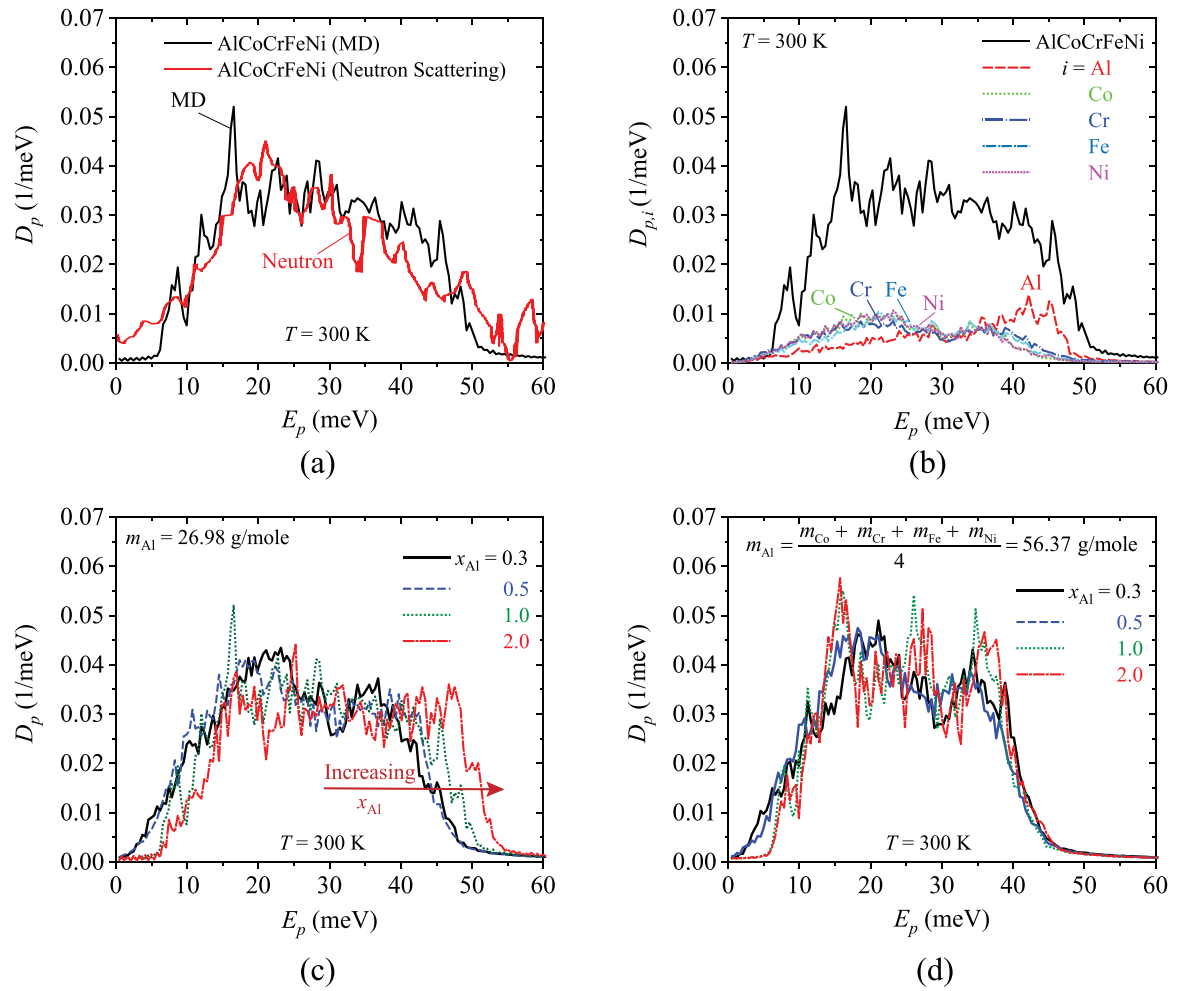
Fig. 3. (a) Phonon density of states (D_p) of AlCoCrFeNi (x_{Al} = 1.0) with respect to the phonon energy (E_p) from MD simulation (black solid) and its comparison with neutron scattering experiment (red dashed). (b) Partial D_p of the constituent elements (Al, Co, Cr, Fe, and Ni) of the AlCoCrFeNi HEA. (c) D_ps of Al$_x$CoCrFeNi (x_{Al} = 0.3, 0.5, 1, and 2) with consideration of Al mass mismatch and (d) those without Al mass mismatch at 300 K from MD simulations. (For interpretation of the references to color in this figure legend, the reader is referred to the web version of this article.)
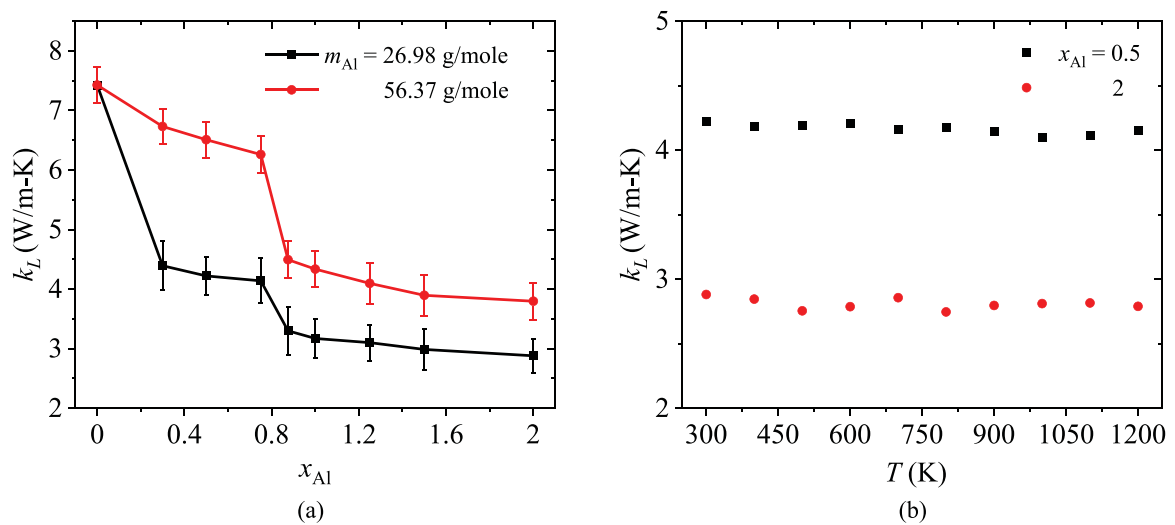

Fig. 4. (a) Lattice thermal conductivity (k_L) with respect to the Al content (x_{Al}) calculated using non-equilibrium MD with and without consideration of Al mass mismatch. (b) Lattice thermal conductivity (k_L) with respect to temperature for FCC (x_{Al} = 0.5) and BCC (x_{Al} = 2.0) cases.

Table 1
Relaxation time approximation for Al$_x$CoCrFeNi ($0 \leq x_{Al} \leq 2$) with a total number of 108 atoms (FCC) and 128 atoms (BCC) at room temperature (300 K).

x_{Al}	Exp. electrical conductivity [22], σ_{exp} ($\times 10^5$ S/m)	AIMD electrical conductivity with a unity of relaxation time, σ/τ ($\times 10^{17}$ S/m-s)	Approximate relaxation time, τ (ps)
0	7.05	13.1	0.382
0.3	8.02	8.25	0.579
0.5	7.40	13.6	0.543
0.75	6.14	7.92	0.846
0.875	6.99	3.10	1.39
1	4.53	3.59	1.26
1.25	5.97	4.70	1.88
1.5	6.52	3.78	1.74
2	4.73	2.95	1.60

mismatch in reducing k_L, especially for small x_{Al}, and also implicates the role of other factors (lattice mismatch and a distribution in bonding strength) in increasing the scattering ($\dot{\gamma}_{Al}$). The initially rapid reduction of k_L, which wanes at higher x_{Al}s, can be explained by Eq. (6) [53]: with the initial inclusion of Al, $\dot{\gamma}_{Al}$ quickly becomes larger than $\dot{\gamma}_{others}$ causing the initial decrease in k_L. At larger x_{Al}, the impact of adding additional Al to an already disordered system are moot, leading to an asymptotic limiting of k_L.

To investigate the possibility of phonon-phonon scattering, the k_L of two HEA cases [$x_{Al} = 0.5$ (FCC) and 2 (BCC)] were simulated at various T's, and showed little dependence on temperature as in Fig. 4b. If interphonon scattering is dominant over other scattering mechanisms, k_L would be expected to decrease with T (as observed in many crystal materials) as a higher T leads to a larger phonon population and more interphonon scatterings. Thus, this T independence demonstrates that scattering by random configurations is more significant than the phonon-phonon scattering in these HEAs.

In addition to suppressing k_L, the electronic properties (k_e, σ, and S) play a critical role in determining the thermoelectric efficiency; these properties are also affected by Al inclusion and are investigated here. The electron relaxation time (τ) for the transport coefficient of each HEA was estimated by comparing the electrical conductivity with the available experimental transport data for Al$_x$CoCrFeNi [22] listed in Table 1. The calculated τ values for BCC HEAs are higher than FCC ones (i.e., more frequent electron scattering). These larger relaxation times indicate less electron scattering in the BCC structures. Therefore, better transport properties are expected at higher Al concentrations.

Using the calculated τ, electrical conductivities (σ) are obtained at different Al contents over a temperature range of 300–1200 K, as shown in Fig. 5a. Electrical conductivity increases as the temperature increases in the BCC structures, while the electrical conductivity of the FCC structures decreases with the temperature. Fig. 5b demonstrates the dependence of the Seebeck coefficient (S) of the HEAs on both temperature and Al concentration. The HEAs examined here show positive S values only at $x_{Al} = 0$ and negative S values for the rest of the HEAs over the temperature range, which represents that
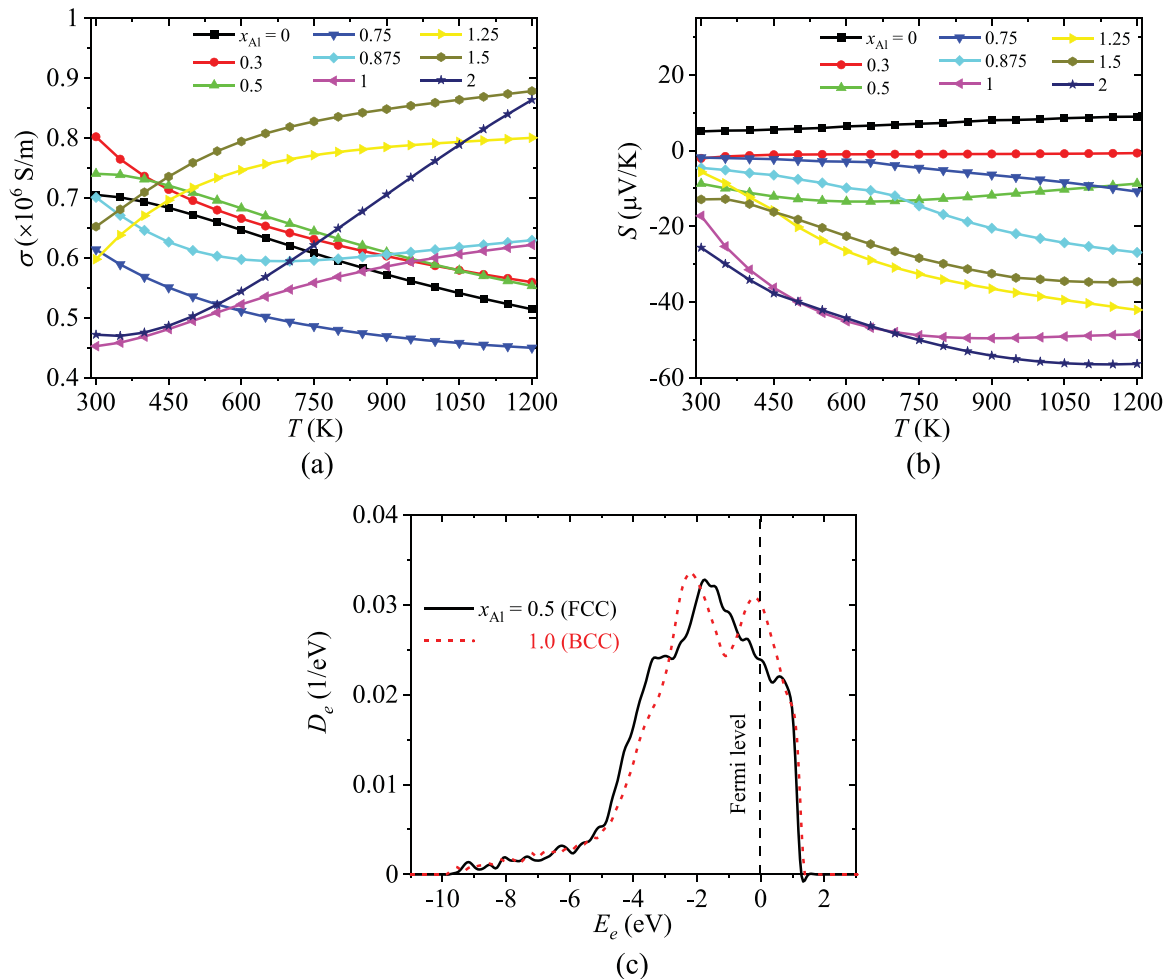

Fig. 5. (a) Electrical conductivity and (b) Seebeck coefficients for Al$_x$CoCrFeNi ($0 \leq x_{Al} \leq 2$) as a function of temperature, (c) Electron density of states for FCC ($x_{Al} = 0.5$) and BCC ($x_{Al} = 1.0$) structures.
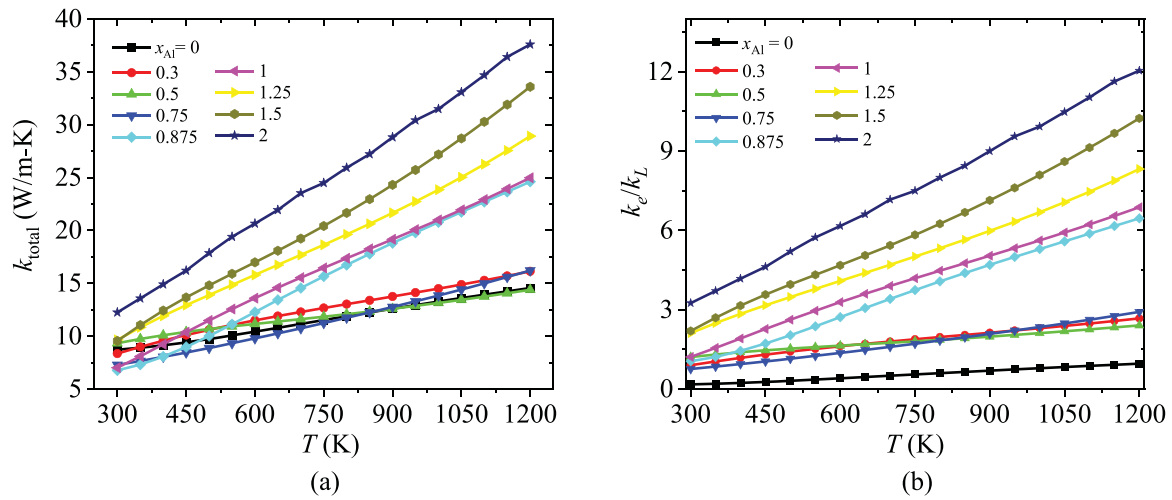
Fig. 6. (a) Thermal conductivity ($k_{total} = k_e + k_L$) and (b) ratio of electronic and lattice thermal conductivity with respect to temperature in $Al_xCoCrFeNi$ ($0 \leq x_{Al} \leq 2$).
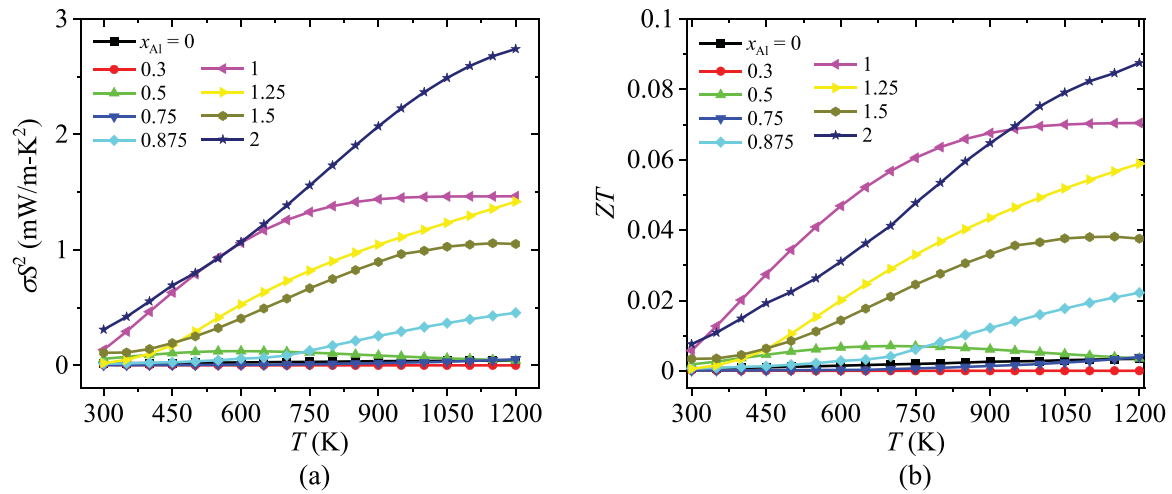

Fig. 7. (a) Power factor (σS^2) and (b) the thermoelectric figure of merit (ZT) with respect to temperature in $Al_xCoCrFeNi$ ($0 \leq x_{Al} \leq 2$).

dominant charge carriers in $Al_xCoCrFeNi$ vary with Al concentration (holes for positive S, while electrons for negative S). Specifically, larger negative S values appear at high temperatures, indicating their n-type semiconducting nature. The absolute value of S increases with temperature in a BCC structure while S value in a FCC structure does not vary significantly. The maximum absolute S value (56.3 μV/K) over our calculated temperature range is found at $x_{Al} = 2.0$ at $T = 1200$ K.

The different temperature dependences of σ and S values in FCC and BCC HEAs can be attributed to different shapes and energy peaks in their electronic density of states from the analysis of the band structures. The larger peak of the electron density of states (D_e) near the Fermi level is found to be higher in the BCC structures, compared to the FCC structures, as illustrated in Fig. 5c. This peak was also observed in other literatures [55–58]. Higher D_e peaks near the Fermi level will allow more electron carriers in the BCC HEAs, increasing electrical conductivity and Seebeck values with the temperature at higher Al contents. Moreover, in both BCC and FCC HEAs, zero band gap was observed in their band structures, demonstrating the metallic characteristics, i.e., the overlapped conduction and valence bands.

The total thermal conductivity (k_{total}) values are calculated by adding the lattice thermal conductivities (k_L) and electronic thermal

conductivities (k_e) from MD and AIMD simulations, respectively. The k_{total} values appear in the range from 6.77 to 37.6 W/m-K over the temperature range of 300–1200 K for $Al_xCoCrFeNi$, as shown in Fig. 6a. The thermal conductivities present an increasing trend with temperature in both FCC and BCC phases due to the increasing k_e, which is attributed to a larger number density of electrons, different from the temperature independence of lattice thermal conductivity. Thus, the electron contribution to the overall thermal transport dominates over the phonon contribution, especially at high temperatures in the BCC $Al_xCoCrFeNi$ (Fig. 6b).

Power factor (σS^2) provides comprehensive electrical performance of the HEAs rather than S or σ alone. Fig. 7a demonstrates that the power factor decreases or maintains constant values at lower x_{Al}s (i.e., FCC crystalline structures) with increasing temperature, while it increases with temperature at higher x_{Al}s with the BCC structure. The thermoelectric power factor is found at $x_{Al} = 2.0$ is 0.31 mW/m-K^2 at 300 K, which significantly increases with the temperature and attains the maximum value of about 2.74 mW/m-K^2 at 1200 K. A combination of larger Seebeck coefficient and higher electrical conductivity leads to a greater power factor in the BCC structures.

Fig. 7b reveals that the temperature dependence of the figure of merit (ZT) is strongly affected by the Al concentration. While the ZT

values at lower Al contents do not vary significantly with temperature, and ZT at higher x_{Al}s increases with T. The maximum ZT value is found for x_{Al} = 2.0 at 1200 K, which is over 25 times higher than the ZT at x_{Al} = 0 at the same temperature. Although the enhanced phonon scattering by a large mass mismatch in $Al_xCoCrFeNi$ contributes to lowering the thermal transport and thus, higher thermoelectric efficiency, it is not a major factor to control thermoelectric performance, different from our initial hypothesis; the dominant factor appears to be the BCC structure. However, the results demonstrate that the significant improvement in the thermoelectricity of the HEAs can be achieved by controlling the light-weight Al content in the $Al_xCoCrFeNi$ HEAs. Furthermore, their high-temperature thermoelectric performance can make them more competitive in the search for new promising thermoelectric materials for future high-temperature applications.

4. Conclusions

Effects of light-weight Al content on the thermoelectric properties of $Al_xCoCrFeNi$ high-entropy alloys ($0 \leq x_{Al} \leq 2$) were investigated over a wide temperature range (300–1200 K) using MD simulations, DFT calculations, and Boltzmann transport theory. As the Al concentration increases, the HEA phase changes from the FCC to BCC structure, and the phonon scattering is largely enhanced by a mass mismatch even with a small Al content, effectively suppressing the phonon transport. Simulations showed that the other thermoelectric properties of $Al_xCoCrFeNi$ HEAs were also strongly dependent on the Al concentration. Larger Seebeck coefficients, electrical conductivities, and electronic thermal conductivities are observed at high x_{Al}s due to the increased electron carriers in the BCC structures, which is supported by the calculation of the electronic band structures and density of states. While the temperature dependence of the phonon transport is not found to be significant due to a minor contribution of interphonon scattering, both the electrical conductivity and Seebeck coefficient increase with temperature, especially at high Al concentrations. This feature allows us to conclude that the thermoelectric performance of $Al_xCoCrFeNi$ HEAs is enhanced by increasing the Al content mainly due to the increase of the thermoelectric power factor at high temperatures, but at low temperatures, the phonon-scattering enhancement by a large atomic mass mismatch is also important. This study will contribute to the design of efficient thermoelectric HEAs for high-temperature applications. Further enhancement is expected to be achieved by more comprehensive evaluation of the HEA's structure and by considering the chemical short-range order and quantification of the random structures. Also, modern data analytics, such as machine learning, can be employed to study a large number of HEAs and predict the thermoelectric performance, thus guiding the experimentalists to design high-performance thermoelectric HEAs effectively.

CRediT authorship contribution statement

Md Abdullah Al Hasan: Methodology, Software, Validation, Formal analysis, Investigation, Data curation, Writing - original draft, Visualization. **Dr. Jiaqi Wang:** Methodology, Investigation, Data curation. **Dr. Seungha Shin:** Conceptualization, Methodology, Writing - original draft, Writing - review & editing, Funding acquisition, Project administration, Supervision. **Dr. Dustin A. Gilbert:** Conceptualization, Funding acquisition, Resources, Investigation, Formal analysis, Writing - review & editing. **Dr. Peter K. Liaw:** Conceptualization, Funding acquisition, Writing - review & editing. **Nan Tang:** Methodology, Investigation, Validation. **W.L. Namila C. Liyanage:** Methodology, Investigation, Validation. **Dr. Louis Santodonato:** Conceptualization, Resources, Writing - review & editing. **Dr. Lisa DeBeer-Schmitt:** Conceptualization, Funding acquisition, Resources, Writing - review & editing. **Dr. Nicholas P. Butch:** Conceptualization, Resources, Writing - review & editing.

Declaration of Competing Interest

The authors declare that they have no known competing financial interests or personal relationships that could have appeared to influence the work reported in this paper.

Acknowledgements

References

[1] H.A. Rahnamaye Aliabad, M. Ghazanfari, I. Ahmad, M.A. Saeed, *Ab initio* calculations of structural, optical and thermoelectric properties for $CoSb_3$ and ACo_4Sb_{12} (A=La, Tl and Y) compounds, Comput. Mater. Sci. 65 (2012) 509–519.

[2] B. Poudel, Q. Hao, Y. Ma, Y. Lan, A. Minnich, B. Yu, X. Yan, D. Wang, A. Muto, D. Vashaee, X. Chen, J. Liu, M.S. Dresselhaus, G. Chen, Z. Ren, High-thermoelectric performance of nanostructured bismuth antimony telluride bulk alloys, Science 320 (5876) (2008) 634–638.

[3] L.E. Bell, Cooling, heating, generating power, and recovering waste heat with thermoelectric systems, Science 321 (5895) (2008) 1457–1461.

[4] J. He, M.G. Kanatzidis, V.P. Dravid, High performance bulk thermoelectrics via a panoscopic approach, Mater. Today 16 (5) (2013) 166–176.

[5] S. LeBlanc, S.K. Yee, M.L. Scullin, C. Dames, K.E. Goodson, Material and manufacturing cost considerations for thermoelectrics, Renew. Sustain. Energy Rev. 32 (2014) 313–327.

[6] D.M. Rowe, CRC Handbook of Thermoelectrics, CRC Press, 2018.

[7] G.J. Snyder, E.S. Toberer, Complex Thermoelectric Materials, Co-Published with Macmillan Publishers Ltd., UK, 2010.

[8] S. Shafeie, S. Guo, Q. Hu, H. Fahlquist, P. Erhart, A. Palmqvist, High-entropy alloys as high-temperature thermoelectric materials, J. Appl. Phys. 118 (18) (2015) 184905.

[9] J. de Boor, T. Dasgupta, H. Kolb, C. Compere, K. Kelm, E. Mueller, Microstructural effects on thermoelectric efficiency: a case study on magnesium silicide, Acta Mater. 77 (2014) 68–75.

[10] S. Chen, K.C. Lukas, W. Liu, C.P. Opeil, G. Chen, Z. Ren, Effect of Hf concentration on thermoelectric properties of nanostructured n-type half-Heusler materials $Hf_xZr_{1−x}NiSn_{0.99}Sb_{0.01}$, Adv. Energy Mater. 3 (9) (2013) 1210–1214.

[11] Q. Shen, L. Chen, T. Goto, T. Hirai, J. Yang, G.P. Meisner, C. Uher, Effects of partial substitution of Ni by Pd on the thermoelectric properties of ZrNiSn-based half-Heusler compounds, Appl. Phys. Lett. 79 (25) (2001) 4165–4167.

[12] S. Populoh, M.H. Aguirre, O.C. Brunko, K. Galazka, Y. Lu, A. Weidenkaff, High figure of merit in (Ti,Zr,Hf)NiSn half-Heusler alloys, Scr. Mater. 66 (12) (2012) 1073–1076.

[13] Y. Zhang, T.T. Zuo, Z. Tang, M.C. Gao, K.A. Dahmen, P.K. Liaw, Z.P. Lu, Microstructures and properties of high-entropy alloys, Prog. Mater. Sci. 61 (2014) 1–93.

[14] O.N. Senkov, J.D. Miller, D.B. Miracle, C. Woodward, Accelerated exploration of multi-principal element alloys with solid solution phases, Nat. Commun. 6 (1) (2015) 6529.

[15] B. Gludovatz, A. Hohenwarter, D. Catoor, E.H. Chang, E.P. George, R.O. Ritchie, A fracture-resistant high-entropy alloy for cryogenic applications, Science 345 (6201) (2014) 1153–1158.

[16] B. Cantor, I.T.H. Chang, P. Knight, A.J.B. Vincent, Microstructural development in equiatomic multicomponent alloys, Mater. Sci. Eng. A 375–377 (2004) 213–218.

[17] J.W. Yeh, S.K. Chen, Y.L. Chen, Novel Alloy Concept, Challenges and Opportunities of High-entropy Alloys, CRC Press, 2007.

[18] D.B. Miracle, J.D. Miller, O.N. Senkov, C. Woodward, M.D. Uchic, J. Tiley, Exploration and development of high entropy alloys for structural applications, Entropy 16 (1) (2014) 494–525.

[19] Y. Pei, X. Shi, A. LaLonde, H. Wang, L. Chen, G.J. Snyder, Convergence of electronic bands for high performance bulk thermoelectrics, Nature 473 (7345) (2011) 66–69.

[20] Y.F. Kao, T.J. Chen, S.K. Chen, J.W. Yeh, Microstructure and mechanical property of as-cast, -homogenized, and -deformed $Al_xCoCrFeNi$ ($0 \leq x \leq 2$) high-entropy alloys, J. Alloy. Compd. 488 (1) (2009) 57–64.

[21] W.R. Wang, W.L. Wang, S.C. Wang, Y.C. Tsai, C.H. Lai, J.W. Yeh, Effects of Al addition on the microstructure and mechanical property of $Al_xCoCrFeNi$ high-entropy alloys, Intermetallics 26 (2012) 44–51.

[22] Y.F. Kao, S.K. Chen, T.J. Chen, P.C. Chu, J.W. Yeh, S.J. Lin, Electrical, magnetic, and Hall properties of $Al_xCoCrFeNi$ high-entropy alloys, J. Alloy. Compd. 509 (5) (2011) 1607–1614.

[23] Y. Shi, L. Collins, R. Feng, C. Zhang, N. Balke, P.K. Liaw, B. Yang, Homogenization of $Al_xCoCrFeNi$ high-entropy alloys with improved corrosion resistance, Corros. Sci. 133 (2018) 120–131.

[24] H.P. Chou, Y.S. Chang, S.K. Chen, J.W. Yeh, Microstructure, thermophysical and electrical properties in $Al_xCoCrFeNi$ ($0 \leq x \leq 2$) high-entropy alloys, Mater. Sci. Eng. B 163 (3) (2009) 184–189.

[25] W. Feng, Y. Qi, S. Wang, Effects of Mn and Al addition on structural and magnetic properties of FeCoNi-based high entropy alloys, Mater. Res. Express 5 (10) (2018) 106511.

[26] S. Li, X. Ni, F. Tian, *Ab initio* predicted alloying effects on the elastic properties of $Al_xHf_{1-x}NbTaTiZr$ high entropy alloys, Coatings 5 (3) (2015) 366–377.

[27] H. Zhang, X. Sun, S. Lu, Z. Dong, X. Ding, Y. Wang, L. Vitos, Elastic properties of $Al_xCrMnFeCoNi$ ($0 \leq x \leq 5$) high-entropy alloys from ab initio theory, Acta Mater. 155 (2018) 12–22.

[28] F. Tian, L. Delczeg, N. Chen, L.K. Varga, J. Shen, L. Vitos, Structural stability of NiCoFeCrAl$_x$ high-entropy alloy from ab initio theory, Phys. Rev. B 88 (8) (2013) 085128.

[29] S. Wang, Atomic structure modeling of multi-principal-element alloys by the principle of maximum entropy, Entropy 15 (12) (2013) 5536–5548.

[30] L. Xie, P. Brault, A.L. Thomann, J.M. Bauchire, AlCoCrCuFeNi high entropy alloy cluster growth and annealing on silicon: a classical molecular dynamics simulation study, Appl. Surf. Sci. 285 (2013) 810–816.

[31] D. Farkas, A. Caro, Model interatomic potentials for Fe–Ni–Cr–Co–Al high-entropy alloys, J. Mater. Res. 35 (22) (2020) 3031–3040.

[32] J. Cai, Y.Y. Ye, Simple analytical embedded-atom-potential model including a long-range force for fcc metals and their alloys, Phys. Rev. B 54 (12) (1996) 8398–8410.

[33] M.A.A. Hasan, J. Wang, Y.C. Lim, A. Hu, S. Shin, Concentration dependence of hydrogen diffusion in α-iron from atomistic perspectives, Int. J. Hydrog. Energy 44 (51) (2019) 27876–27884.

[34] L. Verlet, Computer "experiments" on classical fluids. I. Thermodynamical properties of Lennard-Jones molecules, Phys. Rev. 159 (1) (1967) 98–103.

[35] M.C. Payne, M.P. Teter, D.C. Allan, T.A. Arias, J.D. Joannopoulos, Iterative minimization techniques for ab initio total-energy calculations: molecular dynamics and conjugate gradients, Rev. Mod. Phys. 64 (4) (1992) 1045–1097.

[36] S. Shin, M. Kaviany, T. Desai, R. Bonner, Roles of atomic restructuring in interfacial phonon transport, Phys. Rev. B 82 (8) (2010) 081302.

[37] R.T. Azuah, L.R. Kneller, Y. Qiu, P.L.W. Tregenna-Piggott, C.M. Brown, J.R.D. Copley, R.M. Dimeo, DAVE: A comprehensive software suite for the reduction, visualization, and analysis of low energy neutron spectroscopic data, J. Res. Natl. Inst. Stand. Technol. 114 (6) (2009) 341–358.

[38] J. Fourier, Analytical theory of heat, translated with notes of A. Freeman, 1955.

[39] G. Kresse, J. Furthmüller, Efficient iterative schemes for ab initio total-energy calculations using a plane-wave basis set, Phys. Rev. B 54 (16) (1996) 11169–11186.

[40] P.E. Blöchl, Projector augmented-wave method, Phys. Rev. B 50 (24) (1994) 17953–17979.

[41] J.P. Perdew, K. Burke, M. Ernzerhof, Generalized gradient approximation made simple, Phys. Rev. Lett. 77 (18) (1996) 3865–3868.

[42] M. Methfessel, A.T. Paxton, High-precision sampling for Brillouin-zone integration in metals, Phys. Rev. B 40 (6) (1989) 3616–3621.

[43] S. Nosé, A unified formulation of the constant temperature molecular dynamics methods, J. Chem. Phys. 81 (1) (1984) 511–519.

[44] G.K.H. Madsen, D.J. Singh, BoltzTraP. A code for calculating band-structure dependent quantities, Comput. Phys. Commun. 175 (1) (2006) 67–71.

[45] J. Yang, H. Li, T. Wu, W. Zhang, L. Chen, J. Yang, Evaluation of half-Heusler compounds as thermoelectric materials based on the calculated electrical transport properties, Adv. Funct. Mater. 18 (19) (2008) 2880–2888.

[46] G.K.H. Madsen, Automated search for new thermoelectric materials: the case of LiZnSb, J. Am. Chem. Soc. 128 (37) (2006) 12140–12146.

[47] T. Thonhauser, T.J. Scheidemantel, J.O. Sofo, J.V. Badding, G.D. Mahan, Thermoelectric properties of Sb_2Te_3 under pressure and uniaxial stress, Phys. Rev. B 68 (8) (2003) 085201.

[48] L.J. Santodonato, Y. Zhang, M. Feygenson, C.M. Parish, M.C. Gao, R.J.K. Weber, J.C. Neuefeind, Z. Tang, P.K. Liaw, Deviation from high-entropy configurations in the atomic distributions of a multi-principal-element alloy, Nat. Commun. 6 (1) (2015) 5964.

[49] J.C. Huang, Evaluation of tribological behavior of Al-Co-Cr-Fe-Ni high entropy alloy using molecular dynamics simulation, Scanning 34 (5) (2012) 325–331.

[50] C. Li, M. Zhao, J.C. Li, Q. Jiang, B2 structure of high-entropy alloys with addition of Al, J. Appl. Phys. 104 (11) (2008) 113504.

[51] Z. Tang, M.C. Gao, H. Diao, T. Yang, J. Liu, T. Zuo, Y. Zhang, Z. Lu, Y. Cheng, Y. Zhang, K.A. Dahmen, P.K. Liaw, T. Egami, Aluminum alloying effects on lattice types, microstructures, and mechanical behavior of high-entropy alloys systems, JOM 65 (12) (2013) 1848–1858.

[52] K. Jin, B.C. Sales, G.M. Stocks, G.D. Samolyuk, M. Daene, W.J. Weber, Y. Zhang, H. Bei, Tailoring the physical properties of Ni-based single-phase equiatomic alloys by modifying the chemical complexity, Sci. Rep. 6 (1) (2016) 20159.

[53] Y.K. Weng, A. Yousefzadi Nobakht, S. Shin, K.D. Kihm, D.S. Aaron, Effects of mass and interaction mismatches on in-plane and cross-plane thermal transport of Si-doped graphene, Int. J. Heat Mass Transf. 169 (2021) 120979.

[54] M. Kaviany, Heat Transfer Physics, Cambridge University Press, 2014.

[55] D. Koskimaki, J.T. Waber, Calculation of thermodynamic information based on the density of states curves of two allotropes of iron, NBS, 1971, pp. 741–754.

[56] E.C. Snow, J.T. Waber, The APW energy bands for the body centered and face centered cubic modifications of the 3d transition metals, Acta Metall. 17 (5) (1969) 623–635.

[57] P. Singh, A. Marshal, A.V. Smirnov, A. Sharma, G. Balasubramanian, K.G. Pradeep, D.D. Johnson, Tuning phase stability and short-range order through Al doping in $(CoCrFeMn)_{100-x}Al_x$ high-entropy alloys, Phys. Rev. Mater. 3 (7) (2019) 075002.

[58] L.H. Bennett, Electronic density of states. Special pub., NBS, Washington, DC (USA), 1971.